APPLIED SCIENCES AND ENGINEERING

Electrostatically driven fog collection using space charge injection

Maher Damak and Kripa K. Varanasi*

Fog collection can be a sustainable solution to water scarcity in many regions around the world. Most proposed collectors are meshes that rely on inertial collision for droplet capture and are inherently limited by aerodynamics. We propose a new approach in which we introduce electrical forces that can overcome aerodynamic drag forces. Using an ion emitter, we introduce a space charge into the fog to impart a net charge to the incoming fog droplets and direct them toward a collector using an imposed electric field. We experimentally measure the collection efficiency on single wires, two-wire systems, and meshes and propose a physical model to quantify it. We identify the regimes of optimal collection and provide insights into designing effective fog harvesting systems.

INTRODUCTION

There are more than 1.1 billion people who lack access to safe drinking water worldwide, according to the World Water Council (*1*). Many remote drought-prone coastal areas have little or no rain and prohibitively expensive water transportation costs but have dense fog that occurs on a regular basis (*2*). Fog harvesting is a promising solution to provide clean water in these regions. Areas prone to dense fog formation are usually close to oceans, where fog clouds form over the water and are then transported by the wind (*3*). Fog is composed of tiny droplets with a typical diameter of 10 μm. Researchers have designed various artificial fog harvesting systems, some of which mimic natural fog collection mechanisms in animals and plants (*4*–*11*), and have successfully implemented small-scale fog collectors (*12*–*14*).

The most common design for fog collectors is a mesh that stands perpendicular to the fog-laden wind (*13*, *15*–*17*). Upon impact, droplets stick to the mesh and grow as they coalesce with other incoming droplets. When they reach a critical size, they shed by gravity into a container. Meshes are used because they cause a smaller deviation of the incoming flow streamlines by letting air pass through their openings. Nevertheless, field studies have shown that these meshes typically have very low efficiencies of around 1 to 2% (*17*).

The main mechanisms that limit the efficiency of mesh-based fog collectors are the shedding rate and the aerodynamic deviation of fog droplets. The shedding rate can decrease the efficiency by two mechanisms. Water can clog the mesh openings, making the mesh locally act as a plate. Re-entrainment of the droplets due to wind drag may also occur before these droplets are collected. Researchers have developed coatings to improve the shedding rate, but the overall efficiency of these meshes remained low, around 10% in laboratory setups, suggesting that the main limitation is not the shedding rate (*7*, *9*, *17*).

The main limitation is the aerodynamic deviation of fog droplets, which can occur on two scales: the mesh (aerodynamic efficiency η_a) and individual mesh wires (deposition efficiency η_d). The overall collection efficiency is $\eta = \eta_a\eta_d$. η_a is the number of droplets directed toward the mesh wires divided by the number of droplets that were directed toward the collector far upstream (*15*). It depends on the shading coefficient *SC* (surface fraction of the wires), and it has been shown that an *SC* around 55% gives a maximum η_a (*16*, *17*).

A more significant bottleneck in the fog collection process is the deviation of the droplets around the individual wires. η_d is defined as the ratio of captured droplets to those initially directed toward the wire. The flow through the mesh wires can be modeled as a flow past a cylinder (*18*). Close to the cylinder of radius R_c, in a region of characteristic size R_c, air streamlines start deviating and the flow separates, as schematically shown in Fig. 1A. The ability of droplets to follow streamlines is characterized by the Stokes number, which is the ratio of the droplet inertia to the drag force (*18*). $St = \frac{\tau_{particle}}{\tau_{flow}} = \frac{\text{Inertia}}{\text{Drag}} = \frac{2R_d^2\rho_w U}{9\eta_g R_c}$, where R_d is the droplet radius, ρ_w is the water density, U is the air speed, and η_g is the air viscosity. At low Stokes number, the droplet trajectories follow the streamlines closely, and few droplets are collected. Figure 1B and movie S1 show the air streamlines and droplet trajectories around a cylindrical wire for $St = 0.05$. At high Stokes number, drag forces do not affect the trajectories, and droplets directed toward the cylinder continue along their trajectories and collide with the cylinder. An empirical formula has been established: $\eta_d = \frac{St}{St+\frac{\pi}{2}}$ (*17*). However, large Stokes numbers require very fine meshes, which are difficult to fabricate and lack structural integrity. Hence, low deposition efficiencies remain a significant challenge in fog collection.

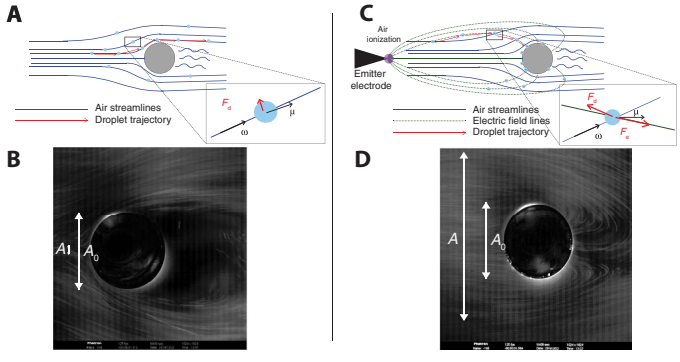

Fig. 1. Trajectories of fog droplets around a cylinder with and without the application of corona discharge. (**A** and **B**) Schematic of air streamlines and droplet trajectories and photograph of droplet trajectories in the absence of an electric field. The inset shows the velocities of the wind $\vec{w}$ and the particle $\vec{u}$ and the drag force acting on the droplet. The bright ring is the edge of the cylinder. (**C** and **D**) Schematic of air streamlines, electric field lines, and droplet trajectories and photograph under corona discharge. Droplets closely follow the electric field lines in this case. The inset shows the additional electric force acting on a droplet. The cylinders in (B) and (D) have a diameter of 1.88 mm.

Department of Mechanical Engineering, Massachusetts Institute of Technology, 77 Massachusetts Avenue, Cambridge, MA 02139, USA.
*Corresponding author. Email: varanasi@mit.edu

Here, we propose to overcome the fundamental aerodynamic limitation of streamline deviation around the collector wires by introducing an additional electric force that will overcome the aerodynamic drag force and propel the fog droplets toward the collector. Active control of droplets with electromagnetic and other fields has recently received significant attention (*19*–*21*). Here, we develop a new approach to enhancing fog collection, inspired by the principles of electrostatic precipitators (*22*–*24*). The mechanism is schematically shown in Fig. 1C. We use an ion emitter to inject a net charge into the droplets (*25*) and use an electric field to direct them toward a collector. The electric field lines go from the emitter to the grounded collector, as shown in Fig. 1C. When the electrical forces are much larger than the air drag forces, the fog droplets follow the field lines and deposit on both sides of the collector wire. We demonstrate this concept experimentally in Fig. 1D and movie S2, which shows that droplets are collected all over the wire and that some droplets that were not initially directed toward the wire are also captured. Intuitively, this suggests that the deposition efficiency, which was previously defined as the fraction of droplets directed toward the wire that are collected, can become greater than one as we will quantitatively show in this paper. The physics of the collection on a single wire will be generalized to a system of two wires and to the more general case of a mesh.

RESULTS AND DISCUSSION

Collection on a single cylindrical wire

The experimental setup is shown schematically in Fig. 2A. A sharp electrode that serves as an ion emitter is placed at a distance L from the horizontal cylindrical wire of radius R_c, which serves as a collector. $L \gg R_c \gg R_d$ (droplet radius). The collector is electrically grounded, while a high voltage V is applied to the emitter electrode, thus establishing an electric field between them. When V is above a critical value V_c (*26*), corona discharge occurs, the air surrounding the emitter is ionized, and a plasma region forms. Electrons are accelerated and have enough energy to ionize the air atoms when they collide with them. A chain reaction occurs, with every collision creating additional electrons and ions. After a collision, the electric field pulls electrons and ions in opposite directions, preventing recombination. At a certain distance from

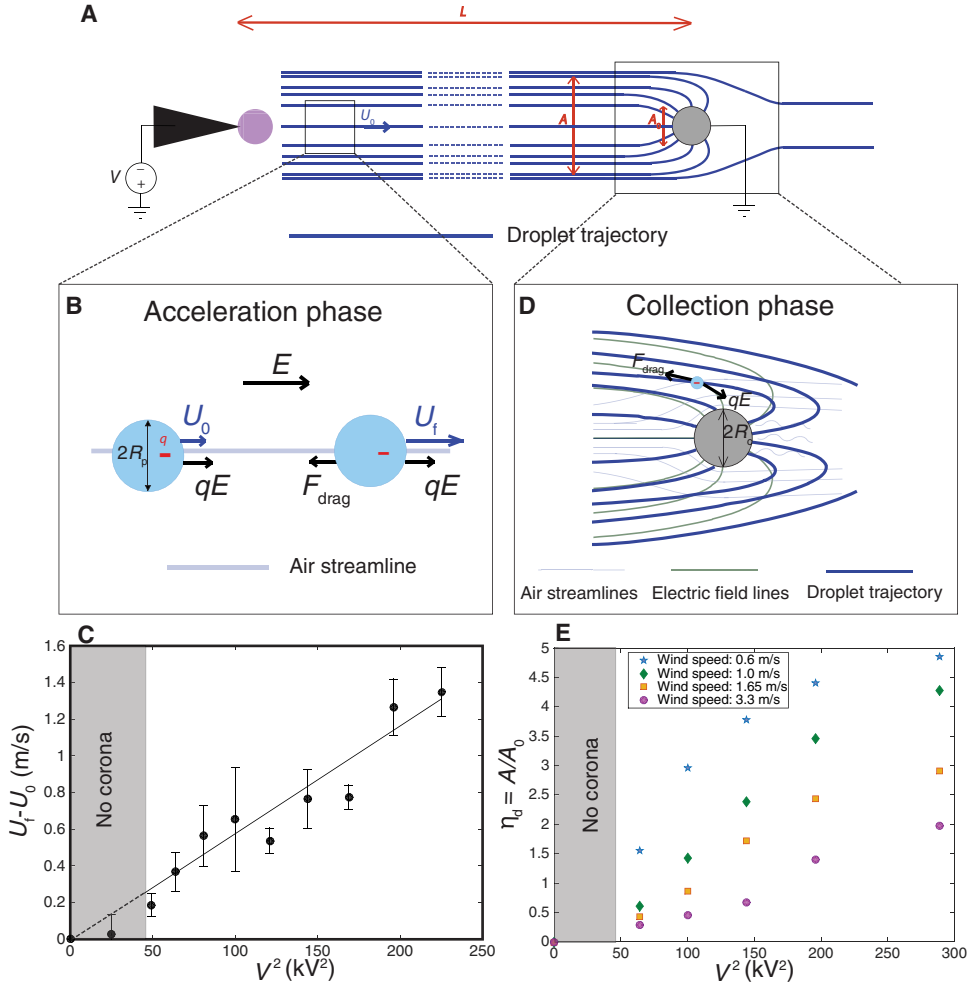

Fig. 2. Mechanism of droplet collection on a cylindrical wire. (**A**) Schematic of simplified experimental setup and droplet trajectories. (**B**) Schematic of the acceleration phase undergone by droplets. The electric field, the initial and terminal velocities, as well as the forces acting on a droplet are shown. (**C**) Added velocity as a function of V^2. A linear fit of the data ($R^2 = 0.94$) gives a slope of 0.006 m/s per kV^2. The gray area is where the voltage is not high enough to induce corona discharge. The error bars reflect the SD over four measurements. (**D**) Schematic of the cross section of the collection phase near the cylinder. Streamlines, field lines, and trajectories of the droplets are shown. (**E**) Nondimensional collection area as a function of V^2 for four different wind speeds. The gray area is where there is no corona discharge.

the emitter, the electric field can no longer provide enough energy to the electrons to sustain the reaction. In this region, ions travel freely in the air toward the opposite electrode, collide with fog droplets, and are captured by them. Thus, the droplets acquire a net charge q of the same polarity as V (*22*, *27*, *28*).

As $L >> R_c$, apart from small regions around the emitter and the collector, the electric field lines are essentially parallel in the central region and the electric field $E \sim \frac{V}{L}$. We assume in the following analysis that the electric field is not disrupted by the presence of fog, and we neglect interdroplet interactions.

In the central region, fog droplets accelerate (Fig. 2B). The droplets enter the region with the wind velocity U_0, and the electric force $F_e = qE$ accelerates them. As their velocity increases, they are subject to a drag force F_d from the air. When $F_e = F_d$, the droplet reaches a terminal velocity U_f.

The equation of motion for the droplet is

$$m\frac{d\vec{u}}{dt} = 6\pi\eta_g R_d(\vec{w} - \vec{u}) + q\vec{E} \quad (1)$$

where $\vec{u}$ is the droplet's velocity, m is its mass, and $\vec{w}$ is the air velocity.

The acceleration time scale $\tau_a = \frac{2}{9}{R_d}^2\frac{\rho_w}{\eta_g}$ is one to two orders of magnitude smaller than the time of flight $\tau_f \sim \frac{d}{U_0}$. Thus, the droplets reach their terminal velocity

$$U_f = U_0 + \frac{qE}{6\pi\eta_g R_d}$$

Figure 2C shows experimental measurements of the added velocity $U_f - U_0$ as a function of V^2. The gray region of the plot corresponds to the case $V < V_c$, where no charge injection occurs. In this regime, the electric force acting on the drops arises because of dielectrophoresis, whose magnitude $\sim \frac{2\pi{R_d}^3\epsilon_0 V^2}{L^3}$ (*29*, *30*) is six orders smaller than that of drag force and, hence, no added velocity is observed. Upon the onset of corona discharge, droplets are charged and the added velocity is proportional to V^2 since both q and E are proportional to V.

As droplets are conductive, the charge is localized at the surface, and the surface charge per unit area can be estimated as $\sigma \sim \epsilon_0 E$ (*31*).

Droplets gain charge when ions attach to them but cannot lose charge to the air (insulator), so the final charge of a droplet is determined by the electric field that it encounters. We can then estimate the surface charge as $\sigma \sim \epsilon_0\frac{V}{L}$, and more precise calculations give $\sigma = 3\epsilon_0\frac{V}{L}$ (see the Supplementary Materials) (*22*).

This calculation is valid here because the time of flight $\tau_f \sim 10^{-2}$s is much larger than the charge relaxation time in the droplet $\frac{\epsilon}{\sigma_w} \sim 10^{-6}$s, where σ_w is the conductivity of deionized water (2.10^{-4}S/m). Thereby, fog droplets have enough time to acquire their maximum charge before they reach the collector (*31*).

Thus, the acquired charge is given by

$$q = 12\pi{R_d}^2\epsilon_0\frac{V}{L} \quad (2)$$

and the added velocity is

$$U_f - U_0 = \left(\frac{2R_d}{\eta_g}\epsilon_0\frac{1}{L^2}\right)V^2 \quad (3)$$

The linear fit to the data in Fig. 2C gives a slope of 0.006. Using the above formula in our case, we find that $U_f - U_0 = 0.008\ V^2$, which matches well with the experimental values, considering the uncertainties in measuring the parameters.

After the acceleration phase, the fog droplets approach the collector wire. In this region (Fig. 2D), both the streamlines and the electric field lines deviate from the parallel configuration. The electric field near the collector scales as $E \sim \frac{V}{R_c}$ (*32*). Near the cylinder, electric forces dominate, but further from the cylinder, the electrical forces are weaker and unable to overcome inertia of the droplets. Therefore, there will be a distance beyond which droplets will not be collected for a given intensity of the applied voltage. Assuming an infinitely long cylinder, the problem reduces to a two-dimensional flow. We then define the area of collection A as the cross-sectional area of the flow of incoming droplets that are collected per unit depth of the cylinder. The deposition efficiency is then $\eta_d = \frac{A}{A_0}$, where A_0 is the area of the cylinder projected in the direction of flow, equal to $2R_c$. We experimentally measured the area of collection for different voltages and wind speeds by imaging the region around the cylinder. Figure 2E presents the nondimensional area A/A_0 as a function of V^2 for different values of U_0. We find that A/A_0 increases with V^2 and decreases with wind speed (fig. S1).

To rationalize these observations, we nondimensionalize Eq. 1 by dividing all distances by R_c, velocities by U_f, and time by $\frac{R_c}{U_f}$, the characteristic time in the collector region (*23*, *33*–*37*)

$$\bar{r} = \frac{r}{R_c},\ \bar{\vec{u}} = \frac{\vec{u}}{U_f},\ \bar{t} = \frac{tU_f}{R_c}$$
$$\frac{d\bar{\vec{u}}}{d\bar{t}} = \frac{1}{St}\left(\bar{\vec{w}} - \bar{\vec{u}}\right) + \frac{Ke}{St}\frac{\vec{E}}{|\vec{E}|} \quad (4)$$

$$St = \frac{2{R_d}^2\rho_w U_f}{9\eta_g R_c};\ Ke = \frac{qE}{6\pi\eta_g R_d U_f}$$

Ke is the ratio of electric and viscous forces, and we will call it the electrical number. Apart from these nondimensional numbers, all the terms of the equation are of order 1. Around the cylinder, E scales as V/R_c and we can use the expressions of q (Eq. 2) and U_f (Eq. 3) to obtain

$$St = \frac{2{R_d}^2\rho_w U_0(1+U^*)}{9\eta_g R_c},\ Ke = \frac{2R_d\epsilon_0 V^2}{\eta_g L R_c U_0(1+U^*)}$$

where we define $U^* = \frac{2R_d\epsilon_0 V^2}{U_0\eta_g L^2}$, a nondimensional number expressing the ratio between the added velocity due to the electric field and the wind velocity.

In the low Stokes number limit (relatively large wires), which is the more practical case, Eq. 4 is further simplified into

$$0 = \left(\bar{\vec{w}} - \bar{\vec{u}}\right) + Ke\frac{\vec{E}}{|\vec{E}|}$$

The electrical number should then govern the physics of the problem, in particular the deposition efficiency. In Fig. 3, we plot A/A_0 as a function of Ke and find that the data for various voltages and wind

speeds collapse into a linear master curve. The single-wire deposition efficiency is given by

$$\frac{A}{A_0} = c.Ke \quad (5)$$

where c can be determined experimentally.

This linear behavior is expected as Ke represents the relative amplitude of the driving force causing the collection.

We explore the limiting cases of Ke. For low U^* (low voltages or high wind speeds), the term containing V^2 in the denominator of Ke is negligible, Ke scales linearly as V^2, and hence, the deposition efficiency increases linearly with V^2. However, for high U^*, U_0 becomes negligible in the denominator and Ke tends toward a constant ($\frac{L}{R_c}$). Any increase in voltage beyond this point does not lead to more collection of droplets. We will call this the voltage saturation. Voltage saturation does not change the linear behavior of the collection rate but limits the maximum reachable Ke. Voltage saturation sets in as Ke approaches this maximum value. Ke can be written as $Ke = \frac{L}{R_c}\frac{U^*}{1+U^*}$. Complete voltage saturation occurs when $U^* >> 1$, but its effects start to be visible when U^* becomes of order 1. U^* ranged here from ~0.05 to ~1.2, and voltage saturation is observed experimentally in the bending of the experimental curves in Fig. 2E for high voltages and low wind speeds, which correspond to the highest U^*. Qualitatively, this limitation in the reachable collection rates arises because, as we increase the voltage, we have a higher electric force that both attracts the droplets and increases their speed, thereby increasing the drag force. Eventually, at high voltages, these two effects balance each other, and the collection cannot be enhanced any further.

Collection on two parallel cylindrical wires

To extend the single-wire model to an array of wires, we now investigate fog collection on a system of two parallel cylindrical wires. We assume that, when the wires are far from each other, air streamlines, electric field lines, and droplet trajectories around each cylinder are not affected by the presence of the other cylinder (Fig. 4, A and B). Thus, the cylinders behave as two single wires. However, when they are close enough, electric field lines and droplet trajectories are influenced by the neighboring wire. When the wires are too close, because of geometric confinement, the droplets above the plane of symmetry are propelled toward the upper wire, while the droplets below go to the lower wire. The deposition efficiency is limited by the system's geometry because of the competition between the two wires over the same droplets, as shown schematically in Fig. 4C. We define two areas of

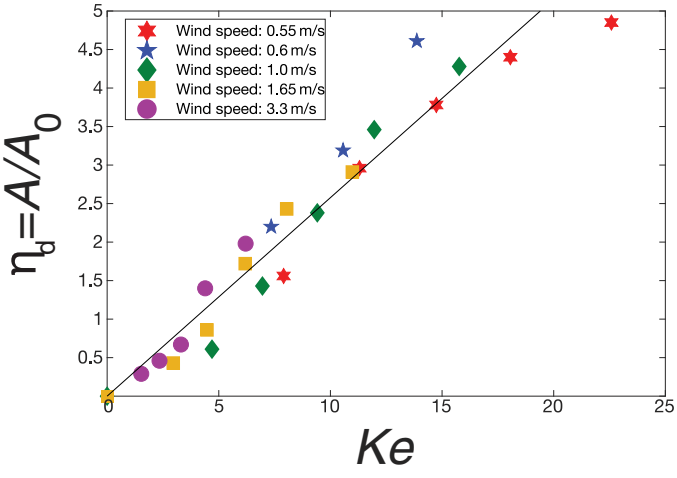

Fig. 3. Dependence of the deposition efficiency on the electrical number. The data correspond to five values of the wind speed and five values of the voltage. The colors represent different wind speeds (red, 0.55 m/s; blue, 0.6 m/s; green, 1 m/s; yellow, 1.65 m/s; purple, 3.3 m/s). The solid line is a linear fit ($R^2 = 0.92$), with a slope of 0.26.

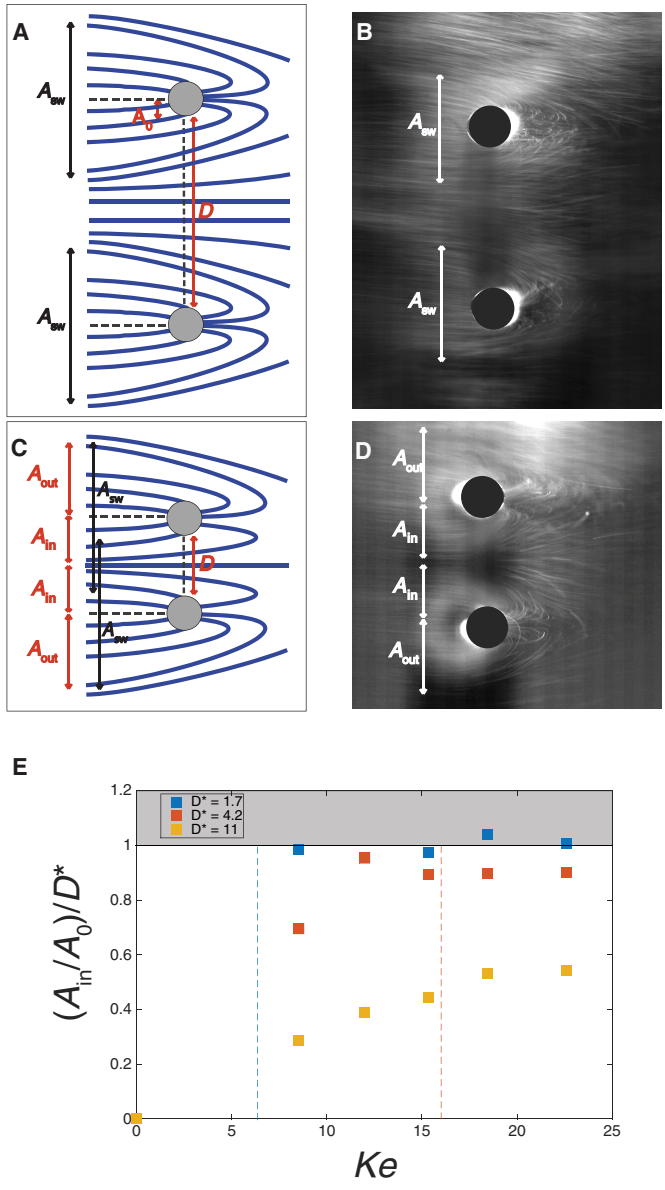

Fig. 4. Mechanism of droplet collection on two parallel cylindrical wires. (**A**) Schematic of droplet trajectories with two distant wires. The collection area of each single wire A_{sw} and the distance D are shown. (**B**) Schematic of droplet trajectories in a two-wire system with spacing saturation. The parameters A_{in}, A_{out}, and D are shown. The white arrows show the single-wire areas of collection A_{sw}. (**C**) Photograph of the droplet trajectories for two distant wires. The wire diameters are 1.88 mm. The distance between them is 10 mm. The applied voltage is 10 kV. (**D**) Photograph of the droplet trajectories in a spacing saturation case. The wire diameters are 1.88 mm. The distance between them is 6 mm. The applied voltage is 14 kV. (**E**) $\frac{A_{in}}{A_0}/D^*$ as a function of Ke for three different wire distances. The gray region covers theoretically inaccessible values. The vertical dashed lines represent the predicted spacing saturation values for $D^* = 1.7$ and 4.2.

collection, A_{in} and A_{out}, accounting for the projected area of the flow of incoming droplets that are collected in the regions between the wires and outside them, respectively. The corresponding deposition efficiencies $\eta_{d,\,in}$ and $\eta_{d,\,out}$ are defined as the ratios of these areas to their respective collection area $A_0 = R_c$.

Figure 4D is a photograph showing the two cylinders and the droplet trajectories, in a case where D is small enough that most of the droplets between the wires are collected. When this happens (small D), a simple geometrical analysis shows that A_{in} reaches a saturation value that is equal to $R_c + \frac{D}{2}$, and $\eta_{d,in} = \frac{A_{in}}{A_o} = D^*$, where $D^* = \frac{D+2R_c}{2R_c}$. We will call this limitation spacing saturation.

We hypothesize that $\frac{A_{in}}{A_o}$ and $\frac{A_{out}}{A_o}$ grow with the single wire law until spacing saturation is reached, at which point A_{in} will plateau, while A_{out} will still follow the single wire law. Knowing that saturation happens when $\frac{A_{in}}{A_o} = D^*$, we can use the single wire law (Eq. 5) to predict the electrical number Ke_{sat} (or equivalently the voltage) or the critical distance D^*_{sat} at which spacing saturation happens.

We experimentally measured A_{in} and A_{out} for different Ke and D^*. The results for A_{in} are reported in Fig. 4E (A_{out} data are reported in fig. S2). We observe that $\frac{A_{in}}{A_o}/D^*$ increases with Ke and plateaus at 1 for low values of D^*. Before the plateau, $\frac{A_{in}}{A_o}$ increases linearly with Ke, with a slope equal to what was measured in the single-wire case (fig. S2). The zone of the graph representing $\frac{A_{in}}{A_o} > D^*$ is inaccessible because of the competition over a finite number of droplets that leads to saturation. The vertical dashed lines represent the expected saturation Ke_{sat} for the cases of $D^* = 1.7$ and 4.2 from our model, and $\frac{A_{in}}{A_o}/D^*$ plateaus beyond these lines for the corresponding curves.

For $D^* = 11$, spacing saturation is not observed here and is expected to occur at a much higher Ke. However, in our case, such a high Ke cannot be reached because of the voltage saturation, which will then become the limiting factor here.

Collection on meshes

Having rationalized the behavior of two parallel wires, we studied the macroscopic collection on the ultimate system of interest: meshes. We conducted similar experiments on 5 cm × 5 cm meshes, and we measured the mass of the collected water after 5 min of exposure. We used five meshes that had the same wire radius, but the spacing D between the wires increased from mesh 1 to mesh 5 (details in Materials and Methods). We quantified the efficiency of the collection process as the ratio of the collected mass to the total mass of water directed toward the mesh $\eta = \frac{m_{collected}}{m_{total}}$. As stated before, $\eta = \eta_a \eta_d \eta_s$, where $\eta_d = \frac{A}{A_0}$ is the deposition efficiency. de Dios Rivera have studied the aerodynamic efficiency previously (*16*), and it is given by $\eta_a = \frac{SC}{1+\left[1.22\left(1.3\,SC+\left(\frac{SC}{1-SC}\right)^2\right)\right]}$, where SC is the shading coefficient. While wettability can improve the shedding efficiency η_s in passive collectors by facilitating shedding and preventing clogging and re-entrainment (*17*), its effect here is minimal. Re-entrainment was not observed in any of our experiments. Some local clogging was observed. In passive inertial collectors, clogging of pores leads to a local deviation of the flow and loss of fog droplets that pass through the neighboring openings. However, droplets here are charged and attracted to the collector, so they can still be collected even if they are deviated and pass through another opening. Therefore, the influence of local clogging is minimal and we took $\eta_s \sim 1$ for all cases.

It should be noted that m_{total} was taken as the quantity of fog generated by our fog machine and does not take into account evaporation and losses of fog before reaching the mesh. Thereby, the reported efficiency is a lower bound for the actual efficiency.

The collection on meshes with corona discharge is drastically increased. As shown in Fig. 5 (A and B) and movies S3 and S4, when there is no corona discharge, there is hardly any collection on the mesh, and the collection beaker remains empty. In contrast, when a corona discharge is established, the mesh is covered with water within a few seconds, and the collection beaker (30 ml) is filled within 30 min. Longer experiments of up to 10 hours were also performed and showed a steady performance (fig. S3)

Figure 5C shows the mass of collected water after 5 min of exposure for different Ke values. The mass m increases with Ke for all meshes. We notice that the mesh with the highest collection is not the one with the highest wire density; mesh 2 has fewer wires but still collects more water because of a higher aerodynamic efficiency. Finally, the collection of meshes 1 and 2 starts to slow down at high Ke, which is due to spacing saturation.

Finally, we plotted the deposition efficiency $\eta_d = \frac{1}{\eta_a}\frac{m_{collected}}{m_{total}}$ for the cases below voltage saturation as a function of Ke in Fig. 5D. We see that the data collapse around a linear curve, which shows that our models for single and double wires can be extended to meshes. The slope is lower than that for the case of a single wire, which may be due to evaporation and leaks as well as the nonuniform distribution of fog across the mesh. Still, η_d reaches values over 2 and can therefore compensate for other inefficiencies and lead to a significantly high overall efficiency for the collection system.

While the operating voltages that we are using are on the order of 10 kV, the current is low and on the order of 0.01 mA. The power consumption in our experimental setup is thus ~0.1 W for a 5 cm × 5 cm mesh, which translates to about 40 W/m^2. Given the output of our experimental system (>60 g/hour), the energy consumption is on the order of 2 kWh/m^3, which is less than current reverse-osmosis desalination consumption (~3 to 5 kWh/m^3). In addition, the power consumption is due to the formation and transport of ions. It does not depend on the presence of fog. In particular, one of the major applications of this study is the recovery of water from cooling tower plumes in power plants, where fog is much more concentrated and is on the order of 5000 liters/m^2 per day. In that case, the energy consumption is estimated to be ~0.2 kWh/m^3, which is one to two orders of magnitude lower than the energy consumption to produce clean water from conventional sources.

In practice, for a given mesh, we can use our scaling law to predict the deposition efficiency as a function of ambient conditions. We have shown that four nondimensional numbers govern the problem: St, Ke, U^*, and D^*. η_d depends on the first two numbers and, in the case of low St, η_d is proportional to Ke. U^* and D^* predict two important limitations, which are the voltage and spacing saturations. We can adjust the voltage according to wind speed and droplet size to maintain a constant throughput of harvested fog water. When designing an active collection mesh, our model also offers design guidelines for the wire size, wire spacing, and operating voltage that should be chosen so as to remain below the voltage saturation and the spacing saturation in typical operating conditions to maximize collection while conserving energy. This method may be combined with other techniques, such as surface treatment of the collector, to slightly enhance the efficiency. These results can be used to design efficient fog harvesters in drought-prone areas to collect water for drinking, irrigation, and afforestation. It is also possible to apply this method to power plant cooling towers to recover water that is lost in

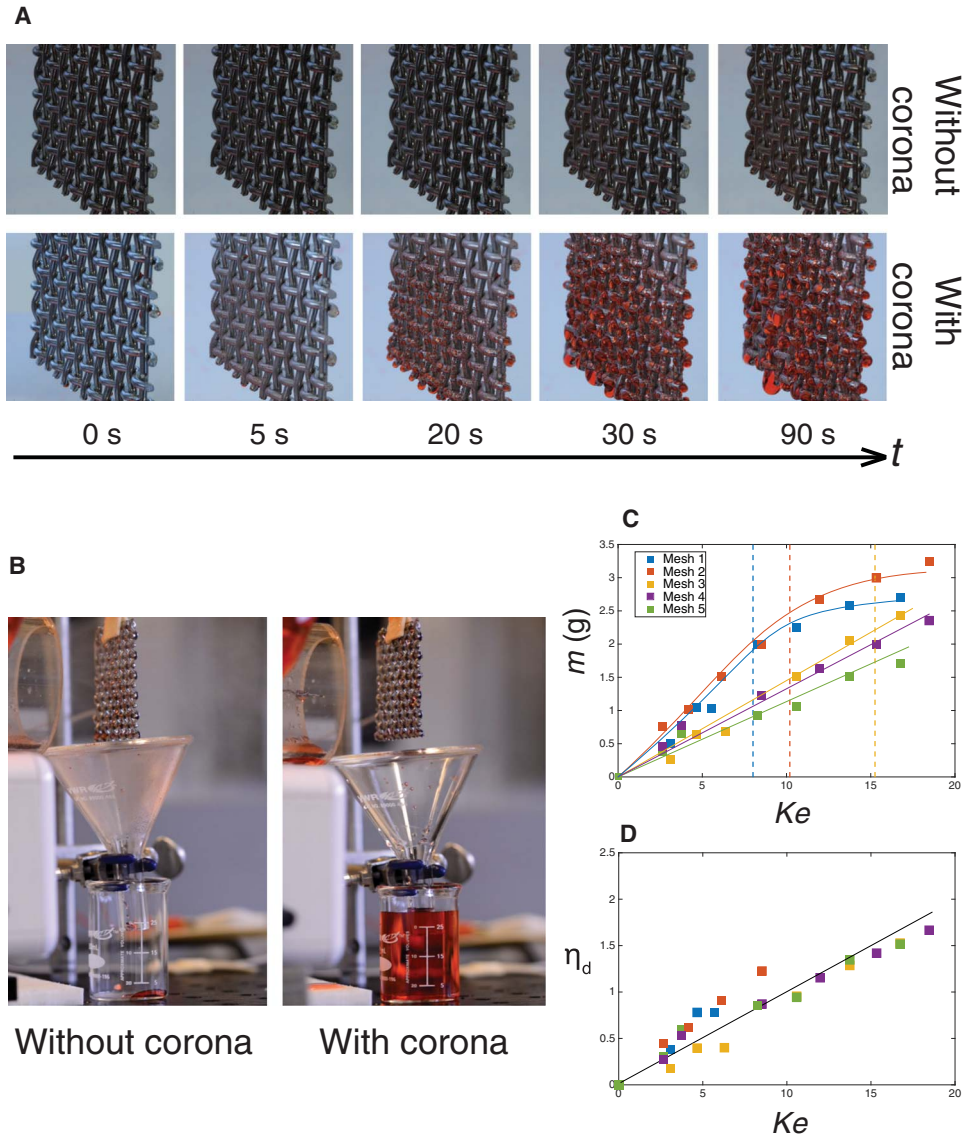

Fig. 5. Fog collection on meshes. (**A**) Snapshots of meshes at different time intervals of fog exposure. In the first row, a 15-kV voltage was applied, while there was no electric field in the second row. Red dye was added to the dispersed fog for visualization purposes. (**B**) Photographs showing the collection mesh and the storage beaker for collected water after 30 min of exposure. The case with high voltage resulted in the collection of 30 ml of water, while only three droplets were collected without electric field. Complete video of collection is shown in movies S3 to S4. (**C**) Mass of the collected water as a function of *Ke* for different meshes. The vertical dashed lines represent the predicted onset of spacing saturation from the two-wire model for meshes 1 to 3. (**D**) Deposition efficiency of the five meshes as a function of *Ke*. The colors represent different meshes according to the color code of (C).

the plumes. Fog removal systems to increase visibility on roads and airports may also be designed.

MATERIALS AND METHODS

Experimental setup and procedure

Samples were placed 4 cm away from the outlet, perpendicular to the axis, of two concentric cylinders (inner diameters, 6.3 and 5 cm) from which came a uniform stream of fog. The fog consisted of a cloud of air-suspended water droplets of an average radius of 3.5 μm, generated using an ultrasonic humidifier (Air-O-Swiss AOS 7146) delivering a volume rate of up to 0.1 liters/hour. The average droplet size was measured with high-magnification imaging of fog droplets. Fog was generated directly into the smaller cylinder through an orifice. Fog was released upstream of the emitter. The fog droplets, the emitter, and the collector were all at the same temperature (room temperature), and the relative humidity in fog conditions was close to 100%. These are also the typical conditions in practical applications. A speed-tunable fan (Thermaltake Mobile Fan II External USB Cooling Fan) was placed at the inlet of the larger cylinder to create the airflow that would convect the fog toward the collection area. A honeycomb flow straightener (Saxon Computers 120mm Honeycomb Airflow Straightener) was placed after the fan to ensure that the wind velocity was uniform through the area of the cylinder, thus reproducing real-fog conditions. The outlet velocity was measured with an anemometer (Testo 405 Hot Wire Thermo-Anemometer) and was spatially uniform within a 15% interval.

Table 1. Characteristics of meshes.

Mesh	Wire diameter (mm)	Opening size (mm)	*D**	Open area (%)
Mesh 1	1.6	1.57	1.98	25
Mesh 2	1.6	2.6	2.65	39
Mesh 3	1.6	4.75	3.97	56
Mesh 4	1.6	6.86	5.29	66
Mesh 5	1.6	11.10	7.94	76

Corona discharge was produced by placing a sharp metallic needle inside the cylinders, its tip coinciding with the outlet of the smaller cylinder. The needle was connected to a high-voltage generator (Spellman SL600) delivering voltages from 0 to −25 kV. Corona discharge was observed to start at a voltage around −7 kV. The onset of corona was detected by the sudden increase in current as ions were generated and traveled between the two electrodes and by the sudden change in the flow pattern of fog. In all experiments, the collector was connected to the ground, its voltage at 0 V. All experiments were performed under ambient temperature and humidity conditions. The collection area was determined from measuring the radius at which the limit between trajectories of collected drops and noncollected drops occurs, in photographs like Fig. 1D. We used five different photographs for each case to do the measurements, and we reported the average area.

Wires and meshes

In single- and two-wire experiments, cylindrical needles, made of stainless steel, with a length of 4 cm and a diameter of 1.88 mm, were used as collectors.

Five-centimeter square meshes were used for collection tests. They were purchased from McMaster-Carr (Corrosion-Resistant Type 304 Stainless Steel Wire Cloth), and their individual characteristics are given in Table 1.

SUPPLEMENTARY MATERIALS

Supplementary material for this article is available at http://advances.sciencemag.org/cgi/content/full/4/6/eaao5323/DC1

Supplementary Text

fig. S1. Nondimensional collection area as a function of the inverse of wind speed for five different voltages.

fig. S2. Nondimensional collection area for two wires as a function of *Ke* for three different wire distances.

fig. S3. Continuous 10-hour fog collection experiment.

movie S1. Droplet trajectories in the absence of an electric field.

movie S2. Droplet trajectories with corona discharge.

movie S3. Ninety-second video of fog collection on meshes with and without corona discharge.

movie S4. Thirty-minute video of fog collection on meshes with and without corona discharge.

REFERENCES AND NOTES

1. World Health Organization, *Meeting the MDG Drinking Water and Sanitation Target: The Urban and Rural Challenge of the Decade* (World Health Organization, 2006).
2. I. Lekouch, M. Muselli, B. Kabbachi, J. Ouazzani, I. Melnytchouk-Milimouk, D. Beysens, Dew, fog, and rain as supplementary sources of water in south-western Morocco. *Energy* **36**, 2257–2265 (2011).
3. O. Klemm, R. S. Schemenauer, A. Lummerich, P. Cereceda, V. Marzol, D. Corell, J. van Heerden, D. Reinhard, T. Gherezghiher, J. Olivier, P. Osses, J. Sarsour, E. Frost, M. J. Estrela, J. A. Valiente, G. M. Fessehaye, Fog as a fresh-water resource: Overview and perspectives. *Ambio* **41**, 221–234 (2012).
4. W. J. Hamilton, M. K. SEELY, Fog basking by the Namib Desert beetle, *Onymacris unguicularis*. *Nature* **262**, 284–285 (1976).
5. Y. Zheng, H. Bai, Z. Huang, X. Tian, F.-Q. Nie, Y. Zhao, J. Zhai, L. Jiang, Directional water collection on wetted spider silk. *Nature* **463**, 640–643 (2010).
6. J. Ju, K. Xiao, X. Yao, H. Bai, L. Jiang, Bioinspired conical copper wire with gradient wettability for continuous and efficient fog collection. *Adv. Mater.* **25**, 5937–5942 (2013).
7. J. Ju, H. Bai, Y. Zheng, T. Zhao, R. Fang, L. Jiang, A multi-structural and multi-functional integrated fog collection system in cactus. *Nat. Commun.* **3**, 1247 (2012).
8. T. H. Means, Fog precipitated by trees. *Science* **66**, 402–403 (1927).
9. A. R. Parker, C. R. Lawrence, Water capture by a desert beetle. *Nature* **414**, 33–34 (2001).
10. D. Seo, J. Lee, C. Lee, Y. Nam, The effects of surface wettability on the fog and dew moisture harvesting performance on tubular surfaces. *Sci. Rep.* **6**, 24276 (2016).
11. L. Zhai, M. C. Berg, F. Cebeci, Y. Kim, J. M. Milwid, M. F. Rubner, R. E. Cohen, Patterned superhydrophobic surfaces: Toward a synthetic mimic of the Namib Desert beetle. *Nano Lett.* **6**, 1213–1217 (2006).
12. R. J. Pilie, W. C. Kocmond, J. E. Jiusto, Warm fog suppression in large-scale laboratory experiments. *Science* **157**, 1319–1320 (1967).
13. R. S. Schemenauer, P. Cereceda, A proposed standard fog collector for use in high-elevation regions. *J. Appl. Meteorol.* **33**, 1313–1322 (1994).
14. S. V. Hering, D. L. Blumenthal, R. L. Brewer, A. Gertler, M. Hoffmann, J. A. Kadlecek, K. Pettus, Field intercomparison of five types of fog water collectors. *Environ. Sci. Technol.* **21**, 654–663 (1987).
15. R. S. Schemenauer, P. I. Joe, The collection efficiency of a massive fog collector. *Atmos. Res.* **24**, 53–69 (1989).
16. J. de Dios Rivera, Aerodynamic collection efficiency of fog water collectors. *Atmos. Res.* **102**, 335–342 (2011).
17. K.-C. Park, S. S. Chhatre, S. Srinivasan, R. E. Cohen, G. H. McKinley, Optimal design of permeable fiber network structures for fog harvesting. *Langmuir* **29**, 13269–13277 (2013).
18. R. L. Panton, *Incompressible Flow* (John Wiley & Sons, 2006).
19. D. Foresti, M. Nabavi, M. Klingauf, A. Ferrari, D. Poulikakos, Acoustophoretic contactless transport and handling of matter in air. *Proc. Natl. Acad. Sci. U.S.A.* **110**, 12549–12554 (2013).
20. K. Piroird, C. Clanet, D. Quéré, Magnetic control of Leidenfrost drops. *Phys. Rev. E Stat. Nonlin. Soft Matter Phys.* **85**, 056311 (2012).
21. D. 't Mannetje, S. Ghosh, R. Lagraauw, S. Otten, A. Pit, C. Berendsen, J. Zeegers, D. van den Ende, F. Mugele, Trapping of drops by wetting defects. *Nat. Commun.* **5**, 3559 (2014).
22. K. Parker, *Electrical Operation Of Electrostatic Precipitators* (IET, 2003).
23. H. F. Kraemer, H. F. Johnstone, Collection of aerosol particles in presence of electrostatic fields. *Ind. Eng. Chem.* **47**, 2426–2434 (1955).
24. H. Uchiyama, M. Jyumonji, Field experiments of an electrostatic fog-liquefier. *J. Electrostat.* **35**, 133–143 (1995).
25. Y. P. Raizer, V. I. Kisin, J. E. Allen, *Gas Discharge Physics* (Springer, 1991), vol. 1.
26. M. Abdel-Salam, D. Wiitanen, Calculation of corona onset voltage for duct-type precipitators. *IEEE Trans. Ind. Appl.* **29**, 274–280 (1993).
27. D. B. Go, R. A. Maturana, T. S. Fisher, S. V. Garimella, Enhancement of external forced convection by ionic wind. *Int. J. Heat Mass Transf.* **51**, 6047–6053 (2008).
28. D. B. Go, S. V. Garimella, T. S. Fisher, R. K. Mongia, Ionic winds for locally enhanced cooling. *J. Appl. Phys.* **102**, 053302 (2007).
29. P. R. C. Gascoyne, J. Vykoukal, Particle separation by dielectrophoresis. *Electrophoresis* **23**, 1973–1983 (2002).
30. T. B. Jones, T. B. Jones, *Electromechanics of Particles* (Cambridge Univ. Press, 2005).
31. J. R. Melcher, *Continuum Electromechanics* (MIT Press, 1981), vol. 2.
32. H. A. Haus, J. R. Melcher, *Electromagnetic Fields and Energy* (Prentice Hall, 1989).
33. A. Jaworek, K. Adamiak, A. Krupa, *Proceedings of the Third International Conference On Multiphase Flow* (ICMF, 1998), pp. 1–10.
34. J. Anagnostopoulos, G. Bergeles, Corona discharge simulation in wire-duct electrostatic precipitator. *J. Electrostat.* **54**, 129–147 (2002).
35. K. S. P. Nikas, A. A. Varonos, G. C. Bergeles, Numerical simulation of the flow and the collection mechanisms inside a laboratory scale electrostatic precipitator. *J. Electrostat.* **63**, 423–443 (2005).
36. H. C. Wang, J. J. Stukel, K. H. Leong, Particle deposition on spheres by inertial and electrostatic forces. *Aerosol Sci. Technol.* **5**, 391–408 (1986).
37. G. Skodras, S. P. Kaldis, D. Sofialidis, O. Faltsi, P. Grammelis, G. P. Sakellaropoulos, Particulate removal via electrostatic precipitators—CFD simulation. *Fuel Process. Technol.* **87**, 623–631 (2006).

Acknowledgments: We thank S. R. Mahmoudi for his contributions to the initial brainstorming for this work. **Funding:** We are grateful for support from the Massachusetts Institute of Technology (MIT) Tata Center for Technology and Design. **Author contributions:** M.D. and K.K.V. conceived the project. M.D. and K.K.V. analyzed the data and wrote the paper. M.D. carried out the experiments. K.K.V. supervised the work. **Competing interests:** M.D. and K.K.V. are inventors on a patent application related to this work filed by the MIT (no. PCT/US2016/054230, filed 28 September 2016). The other authors declare no competing interests. **Data and materials availability:** All data needed to evaluate the conclusions in the paper are present in the paper and/or the Supplementary Materials. Additional data related to this paper may be requested from the authors.

Submitted 31 July 2017
Accepted 24 April 2018
Published 8 June 2018
10.1126/sciadv.aao5323

Citation: M. Damak, K. K. Varanasi, Electrostatically driven fog collection using space charge injection. *Sci. Adv.* **4**, eaao5323 (2018).